

## Numerical simulation and experimental verification of mulch spreading system of paddy field based on CFD

Xiaozhe Yu<sup>1,2</sup>, Mingjin Xin<sup>1</sup>, Yuqiu Song<sup>1</sup>, Jia Xu<sup>3</sup>, Wentao Ren<sup>1\*</sup>

<sup>1</sup>Shenyang Agricultural University, ShenYang 110866, China

<sup>2</sup>Inner Mongolia University For Nationalities, TongLiao 028000, China

<sup>3</sup>Agricultural mechanization technical extension station of beopiao, Chaoyang 122100, China

Corresponding Author Email: [imunyxz@163.com](mailto:imunyxz@163.com)

<https://doi.org/10.18280/ijht.360144>

### ABSTRACT

**Received:** 10 October 2017

**Accepted:** 21 December 2017

**Keywords:**

*numerical simulation, CFD, paddy field  
machiner, experiment.*

In order to realize the technology of mechanized mulching planting in paddy field, the flow of surface soil in paddy field was simulated by using Fluent software, and the flow of air and mud during parallel slide of equipment in two-phase fluid medium of air and mud was studied. The simulation method of the two-phase flow was determined, and the two-phase diagram of air and mud and velocity and pressure diagrams of fluid around the model were obtained. The mud around the model was divided into four regions  $M_q$ ,  $M_c$ ,  $M_x$ ,  $M_s$ . Based on this, the structural parameters of the mulching system were optimized. At the speed of 1.65 m/s and the viscous coefficient of 2.72kg/m·s, Fluent was used in simulation analysis and experimental verification of the four models of soil-engaging equipment in the optimized paddy field mulching system. The results show that: the increase of  $\alpha$ ,  $\beta$  (vertical inclination angle  $\alpha = 150^\circ$  and end embedded angle  $\beta = 150^\circ$ ) can significantly improve the traction resistance and mud obstruction of the equipment. The relative error of the traction resistance of four models of cylindrical roller, elliptical roller, ejector plate and ship plate was 8.3%, 10.27%, 6.67% and 13.74% respectively. The simulation results are in good agreement with the experimental data, which verifies the reliability of the model and provides a new research method for the study on surface soil of paddy field.

## 1. INTRODUCTION

The mulching system is essential to the mechanized application of plastic mulches in rice fields. The main function of the system lies in smoothing the field surface and paving the degradable mulches before rice transplanting. Currently, most rice mulching machines are transplanters with disseminator removed. In practice, the machine needs to withstand both mud resistance and part of its dead load. For the sake of efficiency, the traction resistance and soil obstruction in the forward direction must be reduced without sacrificing the mulching quality.

Over the years, much research has been done to reduce the mud resistance in mechanical operation [1]. For instance, B. G. Richards et al. [2] established a calculation model for the three-phase features of unsaturated soils, and applied it to explore the nonlinearity, irreversibility and hysteresis of water, solution and material conversion in drylands. Focusing on machine speed and soil shear rate, Karmakar et al. [3] simulated the soil-machine interaction by computational fluid dynamics (CFD), and validated the simulated results with the experimental data. Zhang Rui et al. created a nonlinear mechanical model for soil particles through discrete element simulation, and employed the model to discuss the effect of soil particle movement on the surface of different bulldozing plates [4, 5]. Shi Weidong et al. [6, 7] developed a mechanical model for cohesive soil, and numerically simulated the acting force between cohesive soil and corrugated bulldozing plate.

With the aid of five numerical simulation methods (e.g. the CFD and Discrete-element method (DEM)), Cao Zhonghua et al. [8] carried out a dynamic simulation of soil trenching contact system, and verified the accuracy of the simulation results. Jiang Mingjing et al. [9, 10] constructed a CFD-DEM coupling model to calculate the fluid and particle motion equations of moistened soil, and investigated the feasibility of the model. Inspired by smooth fluid dynamics, Yang Wang et al. [11, 12] built a dynamic simulation model for rotary soil tillage system, and found that the model is accurate enough to enhance the crushing effect of micro-cultivator. Guo Wei et al. [13] put forward a CFD model for soil and cutter head, and proved it correct and feasible with the tunnelling data in actual engineering.

To sum up, the existing studies on soil-machine interaction and CFD-based soil dynamic models mainly focus on dry lands rather than paddy fields [14, 15]. To make up for the gap, this paper introduces the CFD simulation technique into the design of paddy field mulching system. Specifically, the air-soil two-phase flow in paddy field was constructed in FLUENT, and the soil-engaging components were modelled in SolidWorks. Then, the motion law of the mulching machine in the two-phase medium and the drag and resistance reduction mechanism were simulated and analysed at the driving speed of 1.65m/s. Through the analysis, the design of the mulching system was optimized, shedding new light on soil-machine interaction in paddy fields.

## 2. THEORETICAL CALCULATION

The soil in paddy fields is composed of minerals, organic matters, air, water, etc. These components can be divided into the three phases of solid, gas and liquid, depending on their states [16]. After a piece of paddy field is flooded, the gaps in the plough layer of the mulching system are basically filled with water (Figure 1). The water-containing surface soil will be turned into mud through the levelling operation. The mud can be regarded as a viscous fluid. It is generally agreed that the rheological properties of both clayey soil and paddy soil can be expressed by Burgers' equation [17]:

$$\gamma = \frac{\tau}{G_M} + \frac{\tau}{G_K} (1 - e^{-G_K t / \eta_K}) + \frac{\tau_0}{\eta_M} t \quad (1)$$

Where  $\tau$  is stress;  $t$  is time;  $\gamma$  is strain;  $G_K$ ,  $G_M$ ,  $\eta_K$  and  $\eta_M$  are soil rheological parameters.

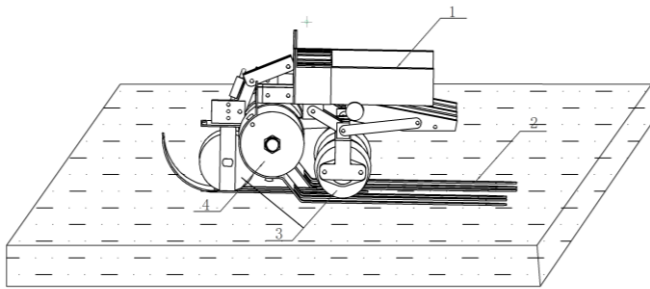


**Figure 1.** Paddy field mulching system

1. Rack; 2. Ship plate; 3. Mulch roller; 4. Fibre container rack

The previous research also shows that the surface mud in paddy fields can be viewed as a fluid, and thus be simulated in FLUENT. Considering the advancing speed of the mulching machine, the speed and flow in turbulence simulation should be included in the solution equation [18-19].

Thus, the control equation of our simulation analysis adopts the momentum conservation equation of standard k- $\epsilon$  two-equation turbulence model.

Momentum conservation equation:

$$\frac{\partial(\rho V)}{\partial t} + \nabla \cdot (\rho V V) = -\nabla p + \nabla \cdot (\tau) + \rho g + F \quad (2)$$

### 2.1 Measurement of mud viscosity

The only premise of fluid analysis lies in the density and viscosity values of the material. Thus, the density and viscosity of the mud in paddy fields were measured at different water contents. According to our previous research, the saturated water content of the soil is 34%; the entire mud layer is saturated, although the water content gradually decreases with the increase of depth. On this basis, the water content of the mud was set to 34.5%, 35%, 35.5%, 36%, 36.5% and 37%, respectively [19, 20].

Before the viscosity measurement, the authors prepared mud samples with the said water contents using the following instruments: a 250mL cylinder, a 10mL cylinder, a 0.1g electronic scale, an infrared drying oven, an NDJ-5S digital viscometer, and several sealing bags. The soil was collected from the paddy fields of Shenyang Agricultural University at the depth of 30cm. The impurities were removed from the soil through drying in the infrared drying oven. Then, 1kg of soil was weighed on the electronic scale, added into the sealing bag, and mixed with a certain amount of water. The water was relocated by the cylinders. After that, the bag was sealed up, labelled, and placed for five days. The same process was repeated to prepare the mud sample of each water content. Before the measurement, the mud in each sealing bag was stirred evenly. During the measurement, the water content of each mud sample was measured three times, and the average viscosity was computed based on the measured results.

**Table 1.** Water contents of mud samples

Mud moisture content /%	34.5	35	35.5	36	36.5	37
Water addition /ml	526.7	538.5	550.4	562.5	574.8	587.3

Note: The water content refers to the amount of water per kilogram of mud.

### 2.2 Results analysis

The results of mud viscosity measurement are listed in Table 2.

**Table 2.** Results of mud viscosity measurement

Water content/%	Test number			Mean viscosity/pa·s
	1	2	3	
34.5	78.42	84.37	79.1	80.63
35	27.16	27.67	28.72	27.85
35.5	7.24	7.46	6.81	7.17
36	4.3	4.51	4.12	4.31
36.5	3.22	3.83	3.87	3.64
37	2.89	2.41	2.86	2.72

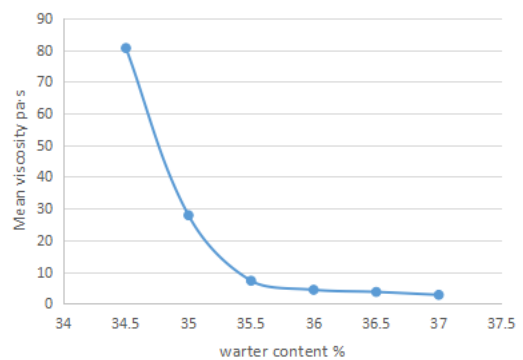


**Figure 2.** Relationship between mud viscosity and water content

As shown in Figure 2, the mud viscosity is negatively correlated with the water content. The viscosity underwent obvious changes when the water content was below 35.5%, and remained relatively stable when the latter was above

35.5%. The trends are attributable to the growing gaps between soil particles with the increase of the water content. The wide gaps turn the soil particles into the discrete state, resulting in a sharp drop in inter-particle cohesion. That is why the mud viscosity remains largely unchanged with the growth in water content [21, 22].

### 3. DEFINITION OF CALCULATION AREA

Based on a fixed 3D coordinate system, a simplified model was created to analyse the motion law of mud in the plough layer under action of the mulching machine. In the coordinate system, the x-axis, y-axis and z-axis respectively point to the vertical side direction, the opposite direction, and the vertical upward direction of machine advancement. The model covers a 7m×3m×2m (L×W×H) cuboid area, 2m below the surface. The inlet and outlet are respectively 2m and 5m away from the area. The left and right sides of the model are of equal distance to the edge of the calculation area.

As shown in Figure 3, the calculation area was meshed into 3.7×10<sup>5</sup> hexahedral grids. The boundaries conditions of the calculation area are as follows: speed inlet boundary conditions for mud and air inlets (1.65m/s, i.e. the maximum advancing speed of the mulching machine along the X-direction), pressure outlet boundary conditions for mud and air outlets, and fixed wall boundary conditions for the walls.

#### 3.1 Calculation results and analysis

It can be seen from Figure 4 that the surface mud gradually accumulated before the mulching machine as the latter moved forward on the paddy field, forming an obstruction effect. The height of the accumulated mud continued to increase over the time, that is, as the mulching machine travelled further into the field. Owing to the relatively high mud viscosity, the height of the mud eventually exceeded that of the machine, such that the accumulated mud flowed over the top of the machine. Since the machine moved on the mud surface, a portion of the mud also passed by both sides of the machine. The height of the mud before and after the machine were different, due to the accumulation of mud in front of the machine. The squeeze force generated in the forward movement, coupled with the gravity of the mud, pushed the part of accumulated mud through the bottom of the machine towards its rear.

Therefore, the mud flow area can be divided into four sub-areas, and the total accumulated amount of mud can be expressed as:

$$M_z = M_q + M_c + M_x + M_s \quad (3)$$

where  $M_z$  is the total amount of mud dragged by the machine;  $M_q$  is the amount of mud accumulated in the front;  $M_c$  is the amount of mud flowing on the two sides;  $M_x$  is the amount of mud flowing through the bottom;  $M_s$  is the amount of mud flowing over the top.

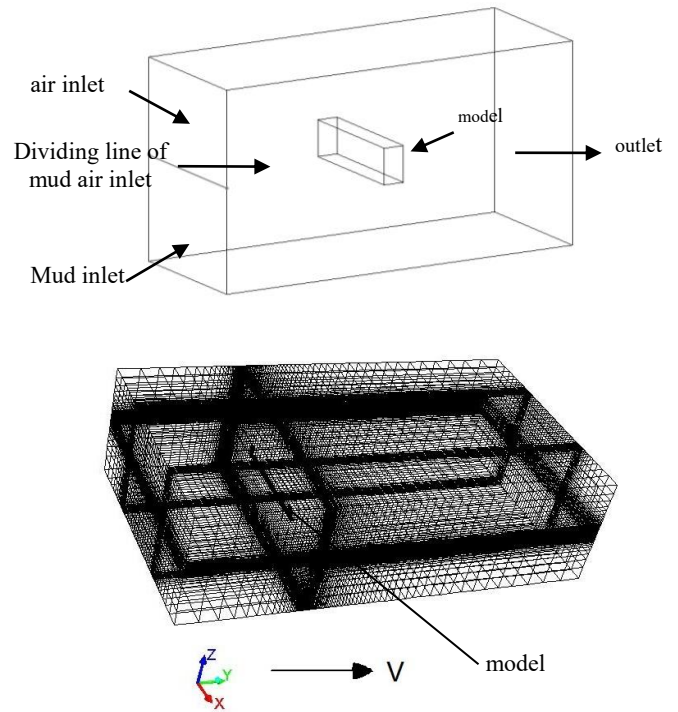


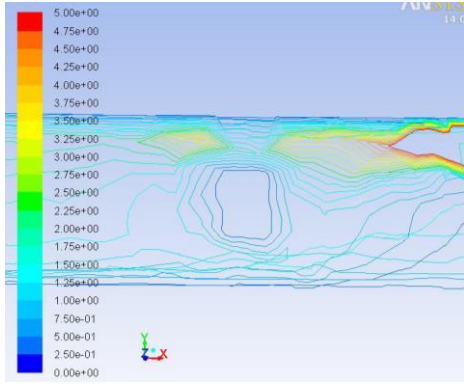
Figure 3. Mesh generation of model and calculation area



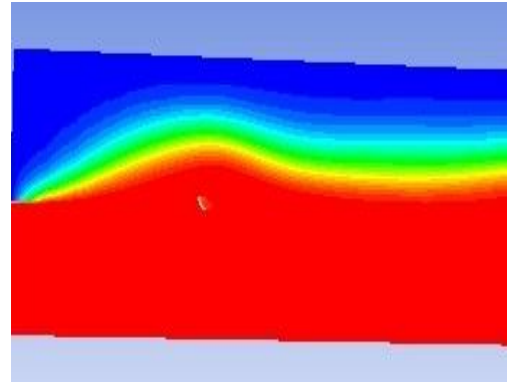
Figure 4. Two phase diagram of air and mud when the mud flows over the mode

#### (1) Speed distribution

As shown in Figure 5, there is an area in which the advancing speed of the machine gradually falls to zero. This is because the accumulated mud continues to impinge on the machine and obstruct its advancement. The flow rate of the mud passing through the bottom of the machine depends on the height difference between the front and rear of the machine, and the squeezing force generated in the forward movement of the machine. The stress pattern can be regarded as a connector with one end under pressure. In the connector, the liquid flow rate mainly relies on the height and pressure differences between liquid levels at both ends. The flow rate is bound to increase to some extent as more and more mud is accumulated in the front. For the mud flowing from both sides, the flow rate also increases to some extent with the increase in the amount and height of mud before the machine.



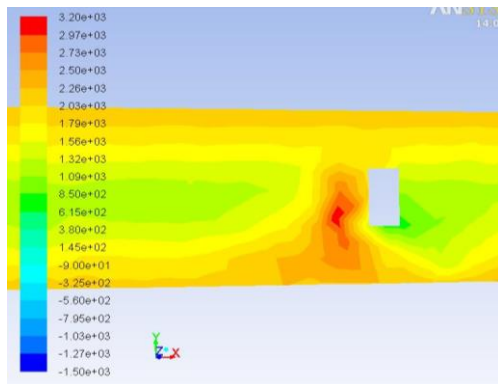
**Figure 5.** Constant velocity diagram when the mud flows over the model



**Figure 7.** Pressure figure around the plate with 0.43s

(2) Pressure distribution

Figure 6 describes the pressure around the model when the mud flows over the machine (the grey box in the middle). In fluid dynamics, a large vortex area will form at the rear of an object in path of the fluid flow. As shown in Figure 5, the advancing speed remains basically the same in a large area to the lower right of the machine, while the speed around this area gradually increases. However, the pressure in the constant speed area Figure 6 is lower than that in the surrounding areas. This means the existence of a vortex in this area. In our model, the upper fluid is air and the lower fluid is mud. The vortex area is relatively low due to the weak fluidity of the mud. Thus, the fluid speed falls gradually from the peripheral of the vortex area to the zero value at the centre of the vortex.



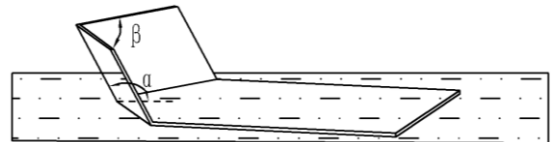
**Figure 6.** Pressure distribution when the mud flows over the model

Figure 7 depicts the distribution of air-mud two-phase flow when the machine has moved 3.4s on the surface of the paddy field. It is clear that the machine is completely submerged in mud. Due to the obstruction of the machine, the mud atop the machine is much taller than it is in other areas. Meanwhile, the front part of the machine differs greatly in shape with the unsubmerged part. The latter part has a gentle shape, because the upper mud has passed over the top of the machine. In this case, the backflow effect of the surface of the unsubmerged part is weakened, and the vortex area moves backwards towards the machine. As the vortex area disappears in the unsubmerged part, the height of the front mud shrinks, forming a gentle transition. By contrast, the upper mud of the front part increases because of the vortex area.

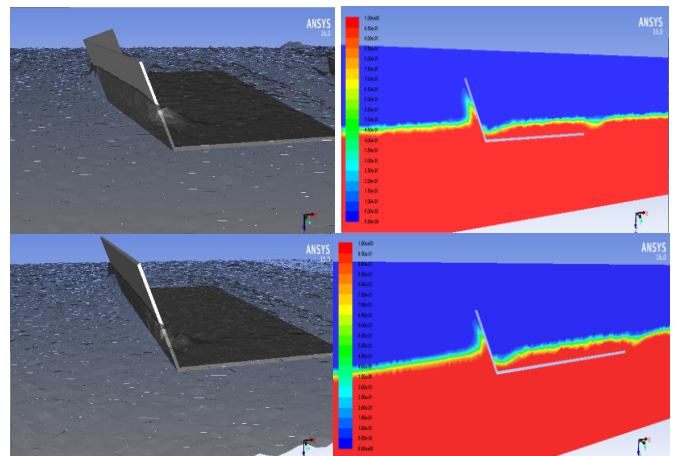
In summary, the mud obstruction and traction resistance will remain at high levels if the  $M_q$  value is excessively high during the operation of the mulching machine. To reduce the  $M_q$  value, the amount of mud accumulated in the front should be adjusted by increasing the values of  $M_c$  and  $M_x$  (the amount of mud flowing through the two sides or the bottom of the machine) or reducing the value of  $M_z$  (the total amount of mud dragged by the machine).

**3.2 Optimization**

The  $M_q$  value can be reduced by increasing the vertical dip angle  $\alpha$  in the forward direction, while the values of  $M_c$  and  $M_x$  can be increased by expanding the end embedded angle  $\beta$ . The values of  $M_q$  and  $M_x$  are also affected by the subsidence of the machine. In light of these, the vertical dip angle  $\alpha$  ( $\alpha=150^\circ$ ) and end embedded angle  $\beta$  ( $\beta = 150^\circ$ ) of the ship plate were increased without changing other structural parameters. To widen the end embedded angle  $\beta$ , the mulch rolls were changed from the conventional cylindrical shape to elliptical cylindrical shape. Then, four modified models for the machine, namely the cylindrical roller model, the elliptical roller model, the ejector plate model, and the ship plate model, were numerically simulated in FLUENT.



**Figure 8.** Structural parameters of the equipment



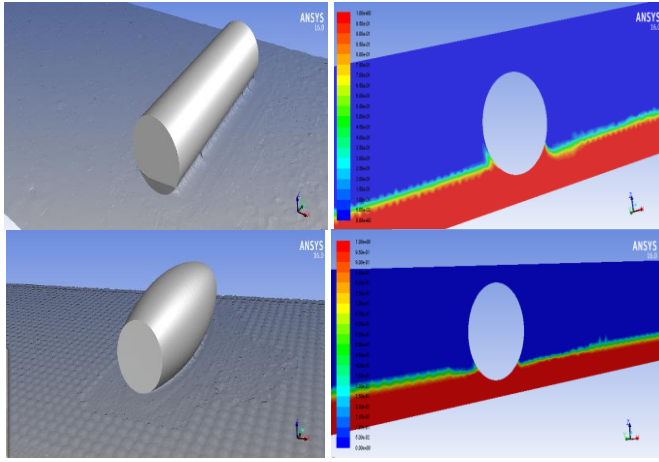


**Figure 9.** Constant velocity diagram when the mud flows over the model

Figure 9 presents the distribution of mud-air two-phase flow of each of the four models as the machine moves towards the mud, in which pure blue means 0 and pure red means 100%. It can be seen that the mud flow on both sides of the ship plate is greater than that of the ejector plate after increasing  $\alpha$  and  $\beta$ , and the mud flow on both sides of the elliptical roller is higher than that of the cylinder roller.

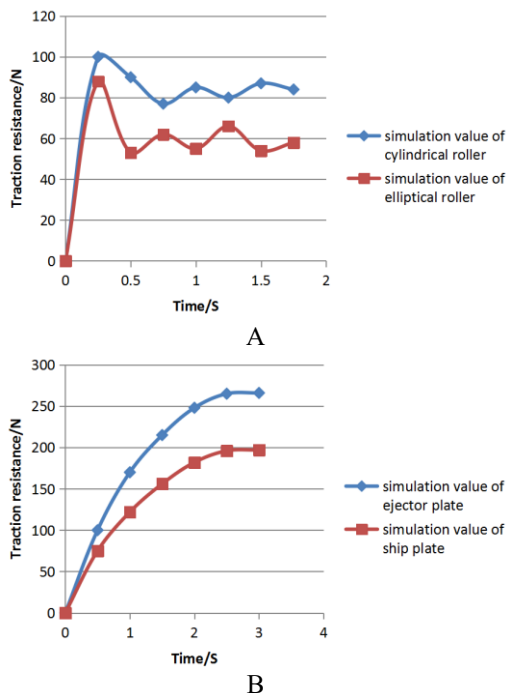


**Figure 10.** Traction resistance-time curves.

As can be seen from Figure 10A, the traction resistances of the two mulch rollers were zero at  $t=0$ . This is because the roller-soil contact belonged to the critical state at the start of the simulation. Then, the traction resistances gradually increased from zero as the machine subsided with the growth in time and load. At about 0.5s, the load reached the peak, and the subsidence of each mulch roller stabilized at 2cm. In this case, the motion of each roller is a combination of rolling and sliding. After that, the traction resistance began to decline, and the dynamic resistance shifted from static friction to dynamic friction. Finally, the traction resistances came to a

stable range at around 0.75s. According to Figure 10B, the initial traction resistances of ejector plate and ship plate were also zero. With the extension in time and growth in load, the traction resistances reached a steady state at around 2.5s, much earlier than those of the two rollers. This is because the two plates, moving in parallel slide, had a larger contact area and greater load from the machine, when the subsidence was stabilized at 2cm.

In general, the traction resistance and mud obstruction of the optimized models are better than those of the original model.

#### 4. EXPERIMENTAL VERIFICATION

To verify the simulation results, the authors carried out several tests in the agricultural lab of Shenyang Agricultural University. The soil box of the tests is 20m long, 0.71m wide and 0.4m deep, with the top edge 0.07m wide on either side. The soil was collected from the paddy fields of Shenyang Agricultural University at the depth of 0~30cm. Before the tests, the soil was crushed to remove the impurities, placed into the soil box, soaked in water for 12h. Then, the soil surface was levelled, following by 12h standing.



**Figure 11.** Test instruments

As shown in Figure 11, the soil box was attached to an electric vehicle, which simulates the speed of the mulching machine. The electric vehicle was connected to an MIK-LCS1 tension and compression sensor and the mulching system through the suspension mechanism. Then, the resistance in the advancement of the mulching system was converted into electrical signals to be captured by the sensor and transmitted to the computer. The test on each model was repeated three times, and the average of the measured data was taken as the final result. For accuracy and repeatability, the mud in the soil box was levelled and the surface was smoothed after each test.

#### 4.1 Results and analysis

Figure 12 shows the variation of the dynamic force of the paddy soil acting on ejector plate and ship plate models. In general, the simulation results are slightly smaller than the experimental data. There are two main reasons for the difference. First, the FLUENT simulation fails to consider the mutual friction between the soil and the wall of the soil box. Second, the paddy soil of the simulation is saturated mud, which can be viewed as a viscous fluid with greater rolling property than the irregular soil particles in actual paddy soil. It can also be observed from the figure that the ejector plate model shares a similar trend of the dynamic force with the ship plate model.

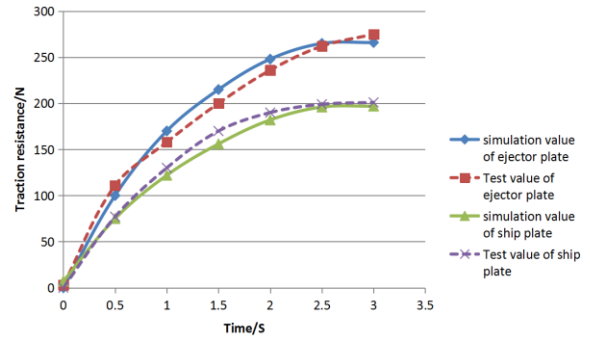


Figure 12. Simulation and experimental results of ejector plate and ship plate

Table 3. Simulation and experimental results

Equipment type	Traction resistance/N				
	simulation value	Test value			Experiment average
cylindrical roller	84.05	88.22	91.51	95.26	91.66
elliptical roller	54.12	55.28	61.54	57.17	57.99
Ejector plate	266.32	291.52	298.66	300.27	296.82
Ship plate	197.15	223.25	227.11	235.32	228.56

Since the traction resistance is stabilized at 3s, the mean resistance at that moment was taken as the result of the CFD simulation. The simulation and experimental results on traction resistance of the four models are listed in Table 3. It is learned that the simulation traction resistances of these models are all close to the experimental values. The relative errors of these models were 8.3%, 10.27 %, 6.67% and 13.74%, respectively. Overall, there is a good agreement between the simulation and experimental results. Thus, the CFD-based soil-machine models are proved reasonable and feasible .

#### 5. CONCLUSION

The soil-machine interaction model for paddy field mulching system was established based on the CFD. The air-mud two-phase flow during the advancement of the machine was simulated in the FLUENT, yielding the speed and pressure distributions of the flow when the mud flows over the machine. Through the analysis of these distributions, the authors obtained the mathematical expression of the mud around the model:  $M_z = M_q + M_c + M_x + M_s$

Based on the mathematical expression, the mulching system was improved by increasing the vertical dip angle  $\alpha$  and end embedded angle  $\beta$ . Then, the improved models were subjected to numerical simulation. It is discovered that the relative errors between the simulation and experimental results of the four models were 8.3%, 10.27%, 6.67% and 13.74%, respectively. The dynamic force curves of ejector plate and ship plate show the good agreement between the simulation and experimental results.

#### REFERENCES

[1] Tong J, Zhang QZ, et al (2014). Finite element analysis and experimental verification of bionic press roller in

reducing adhesion and resistance. Transaction of the Chinese Society for Agricultural Machinery 45(7): 135-140. <https://doi.org/10.6041/j.issn.1000-1298.2014.07.014>

[2] Firuziaan M, Estorff OV. (2003). Simulation of the Dynamic Behavior of Bedding-Foundation-Soil in the Time Domain. 41(2): 385-391. [https://doi.org/10.1007/978-3-540-45476-2\\_21](https://doi.org/10.1007/978-3-540-45476-2_21).

[3] Karmakar S, Kushwaha RL. (2005). Dynamic modeling of soil tool interaction: an overview from a fluid flow perspective. Terramechanics 43(3): 411-425. <https://doi.org/10.1016/j.jterra.2005.05.001>.

[4] Jin T, Zhang QZ, et al. (2017). Effects of bionic geometric structure press rollers on reducing rolling resistance and adhesion against soil. Applied Mechanics and Materials 461: 63-72. <https://doi.org/10.4028/www.scientific.net/amm.461.63>

[5] Kumar K, Delenne JY, Soga K. (2017). Mechanics of gr-anular column collapse in fluid at varying slope angles. Hydrodynamics Research and Progress 29(4): 529-541. [https://doi.org/10.1016/s1001-6058\(16\)60766-7](https://doi.org/10.1016/s1001-6058(16)60766-7).

[6] Meguid MA, Ahmed MR, Hussein MG, Omeman Z. (2017). Earth pressure distribution on a rigid box covered with U-shaped geofoam wrap. International Journal of Geosynthetics & Ground Engineering 3(2): 11-21. <https://doi.org/10.1007/s40891-017-0088-4>.

[7] Park KM, Yoon HS, Min IK. (2017). CFD-DEM based numerical simulation of liquid-gas-particle mixture flow in dam break. Communications in Nonlinear Science & Numerical Simulation 65(1): 125-132. <https://doi.org/10.1016/j.cnsns.2017.11.010>.

[8] Asaf Z, Rubinstein D, Shmulevich I. (2007). Determination of discrete element model parameters required for soil tillage. Soil & Tillage Research 92(1): 227-242. <https://doi.org/10.1016/j.still.2006.03.006>.

[9] Borreani W, Bruzzone M, Chersola D, Firpo G, Lomonaco G, Palmero M, Panza F, Ripani M, Saracco

- P, Viberti CM. (2017). Preliminary thermal-fluid-dynamic assessment of an ADS irradiation facility for fast and slow neutrons. *International Journal of Heat & Technology* 35(Special Issue 1): S186-S190. <https://doi.org/10.18280/ijht.35sp0126>.
- [10] Borreani W, Chersola D, Lomonaco G, Misale M. (2017). Assessment of a 2D CFD model for a single phase natural circulation loop. *International Journal of Heat & Technology* 35(Special Issue 1): S300-S306. <https://doi.org/10.18280/ijht.35sp0141>.
- [11] Bottarelli M, Bortoloni M, Bottarelli M, Bortoloni M. (2017). On the heat transfer through roof tile coverings. *International Journal of Heat & Technology* 35(Special Issue 1): S316-S321. <https://doi.org/10.18280/ijht.35sp0143>.
- [12] Erkinaci T, Baytas F. (2017). CFD investigation of a sensible packed bed thermal energy storage system with different porous materials. *International Journal of Heat & Technology* 35(Special Issue1): S281-S287. <https://doi.org/10.18280/ijht.35sp0138>.
- [13] Ibrahmi A, Bentaher H, Maalej A. (2014). Soil-blade orientation effect on tillage forces determined by 3d finite element models. *Spanish Journal of Agricultural Research* 12(4): 941-951. <https://doi.org/10.5424/sjar/2014124-5766>.
- [14] Xue Z, Liu Q, Emmanuel P, Qin J, Liu D, Gao W, Gong Y, Bai X. (2017). Analysis on the effects of pre-heating temperature on mechanical properties of pellets made from corn stalk powder. *International Journal of Heat & Technology* 35(2): 421-425. <https://doi.org/10.18280/ijht.350227>.
- [15] Caldwell RA, Feeny BF. (2016). Smooth complex orthogonal decomposition applied to traveling waves in elastic media. Springer International Publishing. [https://doi.org/10.1007/978-3-319-30084-9\\_26](https://doi.org/10.1007/978-3-319-30084-9_26).
- [16] Caldwell RA, Feeny BF. (2016). Characterizing wave behavior in a beam experiment by using complex orthogonal decomposition. *Journal of Vibration & Acoustics* 138(4): 431-438. <https://doi.org/10.1115/1.4033268>.
- [17] Kumar K, Delenne JY, Soga K. (2017). Mechanics of granular column collapse in fluid at varying slope angles. *Hydrodynamics Research and Progress* 29(4): 529-541. [https://doi.org/10.1016/s10016058\(16\)60766-7](https://doi.org/10.1016/s10016058(16)60766-7).
- [18] Meguid MA, Ahmed MR, Hussein MG, Omeman Z. (2017). Earth pressure distribution on a rigid box covered with U-Shaped geofabric wrap. *International Journal of Geosynthetics & Ground Engineering* 3(2): 11-20. <https://doi.org/10.1007/s40891-017-0088-4>.
- [19] Obermayr M, Dressler K, Vrettos C, Eberhard P. (2011). Prediction of draft forces in cohesionless soil with the discrete element method. *Journal of Terramechanics* 48(5): 347-358. <https://doi.org/10.1016/j.jterra.2011.08.003>.
- [20] Park KM, Yoon HS, Min IK. (2017). CFD-DEM based numerical simulation of liquid-gas-particle mixture flow in dam break. *Communications in Nonlinear Science & Numerical Simulation* 42(3): 10-21. <https://doi.org/10.1016/j.cnsns.2017.11.010>.
- [21] Rashad A. (2017). Unsteady nanofluid flow over an inclined stretching surface with convective boundary condition and anisotropic slip impact. *International Journal of Heat & Technology* 35(1): 82-90. <https://doi.org/10.18280/ijht.350111>.
- [22] Srinivasacharya D, Shafeeurrhman M. (2017). Joule heating effect on entropy generation in MHD mixed convection flow of chemically reacting nanofluid between two concentric cylinders. *International Journal of Heat & Technology* 35(3): 487-497. <https://doi.org/10.18280/ijht.350305>.